CuTaS₃: Intermetal d–d Transitions Enable High Solar Absorption

Jaeseok Heo,[†] Liping Yu,[‡,∥] Emmeline Altschul,[†] Benjamin E. Waters,[§] John F. Wager,[§] Alex Zunger,[‡] and Douglas A. Keszler*,[†]

[†]Department of Chemistry, Oregon State University, Corvallis, Oregon 97331-4003, United States
[‡]University of Colorado, Boulder, Colorado 80309, United States
[∥]National Renewable Energy Laboratory, Golden, Colorado 80401, United States
[§]School of Electrical Engineering and Computer Science, Oregon State University, Corvallis, Oregon 97331-5501, United States

Ⓢ *Supporting Information*

ABSTRACT: To realize the fundamental limits of photovoltaic device efficiency, solar absorbers must exhibit strong absorption and abrupt absorption onsets. Ideally, onsets to maximum absorption ($\alpha > 10^5$ cm^{-1}) occur over a few tenths of an electronvolt. First-principles calculations predict CuTaS₃ represents a potentially new class of materials with such absorption characteristics. Narrow metallic d bands in both the initial and final states present high joint densities of states and, therefore, strong absorption. Specifically, a mixture of metal d (Cu^{1+}, d^{10}) and S p characterizes states near the valence band maximum, and metal d (Ta^{5+}, d^0) dominates near the conduction band minimum. Optical absorption measurements on thin films confirm the abrupt onset to strong absorption $\alpha > 10^5$ cm^{-1} at $E_g + 0.4$ eV ($E_g = 1.0$ eV). Theoretical CuTaS₃ solar cell efficiency is predicted to be 28% for a 300 nm film based on the metric of spectroscopic limited maximum efficiency, which exceeds that of CuInSe₂. This sulfide may offer new opportunities to discover and develop a new class of mixed d-element solar absorbers.
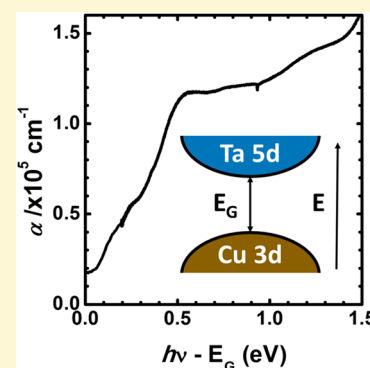
INTRODUCTION

We report the discovery of strong solar absorption by the d-band sulfide CuTaS₃,[1,2] and we address why such strong absorption occurs. The findings offer opportunities to improve efficiencies of solar devices.

d-bands shape electronic behavior and, hence, the physical properties of many transition-metal sulfides. Because these bands have minimal dispersion, they produce high densities of states and high joint densities of states. High *joint* densities suggest the potential for elevated optical absorption coefficients, a useful materials property to improve photovoltaic device efficiencies via drift operation.[3−5] In drift operation, the electric field across a thin absorber layer minimizes the adverse consequences of low carrier mobilities and heavy effective masses of carriers in narrow d bands.

Ideally, we would identify materials with narrow metallic d-bands near both the valence band maximum (VBM) and the conduction band minimum (CBM). In binary compounds with a single d-electron element, the only way to create a band gap with d character near the band edges is via symmetry-induced ligand-field splitting of the d orbitals. These characteristics are found in the classic Mott insulators NiO, MnO, CoO, and FeO as well as in binary chalcogenides. Among sulfides, FeS₂[6−8] and MoS₂[9−11] carry these traits, as evidenced by their high optical absorption coefficients $> 10^5$ cm^{-1}. In FeS₂, the octahedral S environment about Fe produces a t$_{2g}$, e$_g$ d-orbital splitting with t$_{2g}$ defining the valence band and e$_g$ the conduction band.[12] The d^6 electron count and low-spin configuration create a filled t$_{2g}$ valence band and an empty e$_g$ conduction band and, thus, a

semiconductor with a band gap near 1 eV. In MoS₂, the trigonal prismatic environment about Mo produces an e′, e″, a$_2$″ d-orbital splitting with e′ defining the valence band.[13] The Mo d^4 electron count fills the valence band to again generate a semiconductor, now with a band gap near 1.9 eV.[9] In general, the semiconductor behavior of FeS₂ and MoS₂ derives from specific coordination geometries coupled to unique electron counts.

To realize new transition-metal chalcogenides with rapidly rising and high absorption, we consider structures with two elements carrying d orbitals, i.e., a ternary option, wherein a d^{10} transition metal defines VBM and a d^0 transition metal, CBM. Here, the band gap arises from an absolute-energy difference between the d orbitals of two chemically distinct transition metals, not from the symmetry splitting of the orbitals of a single transition-metal atom. Since Cu d^{10} atomic orbitals are energetically far deeper than the d^0 orbitals[14−16] (as gleaned also from the absolute solid-state energies),[17,18] band gaps should exist between d^{10} Cu^{1+} and d^0 Group 4, 5, and 6 transition metals. Hence, materials with d^0 and d^{10} elements should enable strong intermetal optical transitions without the symmetry and band gap restraints of single d-metal systems. Naturally, chalcogenide p orbitals blend with the d orbitals to

further enhance transition strength. From these considerations, we identified $CuTaS_3$ as a potentially strong absorber and set out to assess its optical and electronic properties computationally and then to confirm them experimentally.

$CuTaS_3$ also brings advantages of low toxicity,[19] material abundance,[20] and low cost.[21] Prior reports have focused only on its preparation and crystal structure.[1,2]

CALCULATION METHODS

Electronic Structure Calculations. All calculations were performed via density functional theory (DFT) and the plane-wave projector-augmented wave (PAW) method,[22,23] as implemented in the VASP code.[24] The atomic positions were relaxed by the Heyd−Scuseria−Ernzerh hybrid functional (HSE06)[25] until all atomic forces were less than 0.02 eV Å^{-1}, with lattice parameters fixed to experimental values. The band structure and optical absorption coefficients were calculated with the many-body GW approximation[26] perturbatively on the top of wave functions and energy eigenvalues calculated from HSE06, i.e., G_0W_0+HSE06). An energy cutoff of 300 eV and Γ-centered homogeneous $3 \times 3 \times 8$ k-mesh were used. Weak spin−orbit coupling effects were not included in the calculations.

Spectroscopic Limited Maximum Efficiency.[27] The power conversion efficiency η of a solar cell is defined as $\eta = P_m/P_{in}$, where P_{in} is the total incident solar energy density, and P_m is the maximum output power density. Spectroscopic Limited Maximum Efficiency is a computed η based on numerically maximizing the product of current density J and voltage V. For a solar cell behaving as an ideal diode and illuminated with photon flux I_{sun}, J and V follow from $J = J_{SC} - J_0(1 - e^{eV/kT})$. The first term is the short-circuit current density J_{SC} given by $J_{SC} = e \int_0^\infty \alpha(E) I_{Sun}(E)\, dE$, where e is the elementary charge and $\alpha(E)$ is the photon absorptivity. The second term is the reverse saturation current $J_0 = J_0^{nr} + J_0^r = J_0^r/f_r$, corresponding to the total (nonradiative J_0^{nr} plus radiative J_0^r) electron−hole recombination current at equilibrium in the dark. The fraction of the radiative recombination current f_r is modeled as $f_r = e^{-\Delta/kT}$, where k is the Boltzmann constant, T is the solar cell operating temperature, and Δ is the difference between the minimum band gap and the direct-allowed band gap. For $CuTaS_3$, $f_r = 1$ since $\Delta = 0$. As required by the principle of detailed balance, the rates of emission and absorption through cell surfaces are equal at equilibrium in the dark. Thus, J_0^r is easily calculated from the rate at which blackbody photons from the surrounding thermal bath are absorbed through the front surface, i.e, $J_r = e\pi \int_0^\infty \alpha(E) I_{bb}(E, T)\, dE$, where I_{bb} is the blackbody spectrum at temperature T.

EXPERIMENTAL METHODS

Crystal Growth and Thin-Film Deposition. $CuTaS_3$ single crystals were grown by chemical vapor transport (CVT) from a combination of elements Cu:Ta:S (purity >99.999%; Alfa Aesar) in the ratio 1:1:3.17. The elements were sealed with 40 mg of $I_2(s)$ (99.998%, Alfa Aesar) in an evacuated fused-silica tube having a diameter of 15 mm and a length of 230 mm. The tube was heated in a tube furnace for 2 weeks with the hot end at 750 °C in a temperature gradient of 5 °C cm^{-1} and then cooled at 10 °C h^{-1} to room temperature. Needle-shaped crystals grew at the hot end of the tube, indicative of an endothermic transport reaction. After cooling, the crystals were washed with deionized water to remove excess halide.

$CuTaS_3$ thin-film deposition on fused-silica substrates was initiated via sequential electron-beam evaporation of Cu (24 nm) and Ta (40 nm) layers. These films were then annealed at 650 °C for 1 h with 122 mg of S in evacuated, sealed fused-silica tubes.

Characterization. The crystals were imaged and characterized compositionally with an FEI Quanta 3D dual-beam scanning electron microscope operated at 15 kV. Single-crystal X-ray diffraction data were collected on a Bruker SMART APEX CCD diffractometer at 293 K with Mo Kα radiation (λ = 0.7107 Å). Thin-film X-ray data were collected on a Rigaku Ultima IV diffractometer with a 0.02 rad slit and

Cu Kα radiation (λ = 1.5418 Å). Scans were made between 10 and 70° 2θ at a rate of 1° min^{-1}. The resulting diffraction patterns were compared to those generated from the single-crystal data to verify formation of the desired phase.

The anisotropic resistivity of crystals was characterized with six-terminal ac measurements,[28] where four Au contacts of $10 \times 10\ \mu m^2$ were formed on the sides of the crystals and two Au contacts were formed on the crystal faces containing b-axis. The contacts were extended with a Ag paste for easy probing. For additional optical and electrical measurements, crystals were ground into polycrystalline powders. The resulting powders were pressed into 0.25-in. diameter pellets and then were sintered at 750 °C for 12 h. MgO powder (99.95%; Cerac) served as the white reflectance standard for diffuse reflectance measurements. Room temperature resistivities were measured in the van der Pauw geometry with a LakeShore 7504 measurement system. Majority carrier type was determined from Seebeck measurements with a custom-built system[29] by applying a 5 K temperature gradient to the sample.

Optical transmittance and reflection data for thin films were acquired with a custom-built system comprising Ocean Optics HR400 & NIR256-2.5 spectrometers and a halogen source (DH-2000-BAL).

RESULTS AND DISCUSSION

Crystal and Electronic Structures of $CuTaS_3$. Based on single crystal X-ray diffraction measurements, we confirmed $CuTaS_3$ (space group $Pnma$) adopts the structure previously reported with statistically equivalent unit-cell parameters a = 9.4985(9), b = 3.4983(3), and c = 11.7693(11) and atomic positional parameters (Table S1).[1,2] Figure 1 shows the crystal
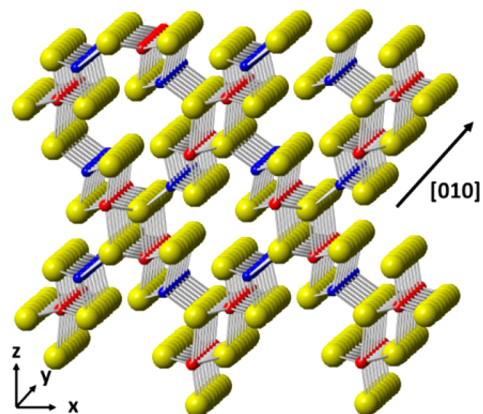

Figure 1. Crystal structure of $CuTaS_3$: Cu, blue; Ta, red; S, yellow.

structure. Cu and Ta occupy distorted tetrahedral and octahedral sites, respectively. The CuS_4 tetrahedra and TaS_6 octahedra independently share edges to form Cu-centered and Ta-centered one-dimensional chains along [010]. Cu atoms and Ta atoms are separated by 3.5 Å along the chain axes. Condensation of these chains then produces an anisotropic structure with −S−Cu−S−Cu−S− and −S−Ta−S−Ta−S− connections only along [010].

Figure 2 shows the calculated band structure. The valence band maximum and the conduction band minimum are both located at Γ, so the material is a direct gap semiconductor with E_g calculated to be 1.3 eV. Bands are flat along Γ−X−S and disperse along S−R−Γ−Y. This disparate dispersion reflects the anisotropy of the crystal structure. The line Γ−X−S predominately represents dispersion along [100] in the crystal structure. Because the Cu-centered chains, like the Ta-centered chains, are isolated one from one another along [100], no significant overlap occurs, so the bands are flat. The line S−
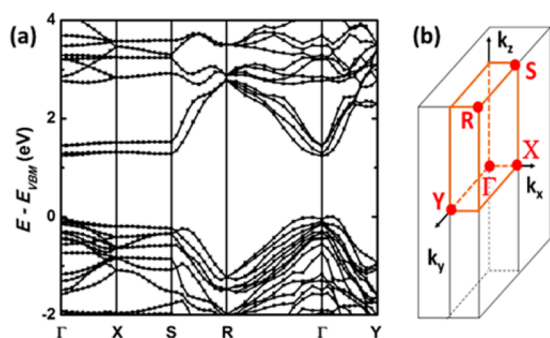
Figure 2. (a) Calculated band structure of CuTaS$_3$; (b) Brillouin zone for primitive cell of CuTaS$_3$.

R−Γ−Y represents dispersion along [010], i.e., the direction of the one-dimensional Cu- and Ta-centered chains where orbital overlap is significant.

Figure 3 shows total and projected densities of states. A mixture of Cu 3*d* and S 3*p* orbitals characterizes the valence
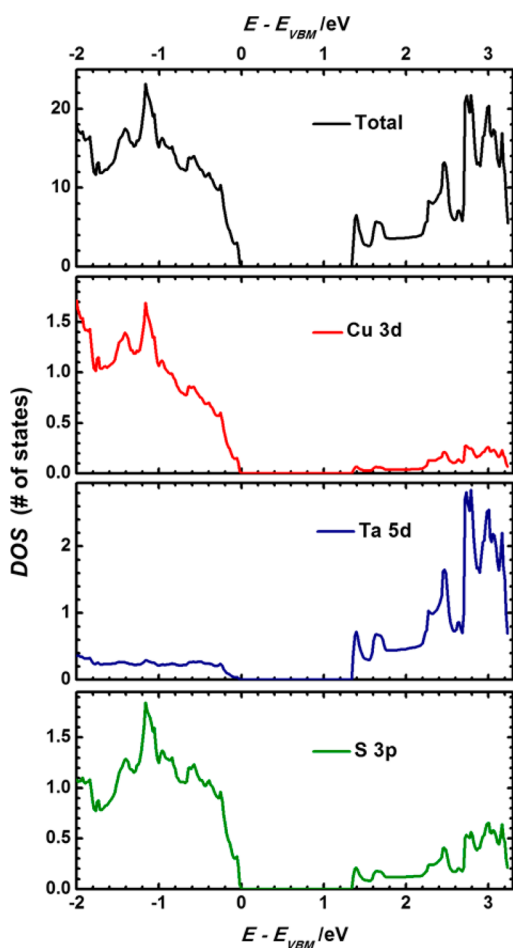

Figure 3. Total and projected densities of states for CuTaS$_3$.

band, while Ta 5*d* dominates the conduction band. Hence, the electronic structure fulfills the design principle for *d* states from two different elements, each prevailing near VBM and CBM. The spikes in the densities of states reflect the flat-band portions of the band diagram and one-dimensional character of the crystal structure. Based on the total number of electrons available, the valence band is filled, the conduction band empty.

Consequently, atomic charges are formally Cu^{1+}, Ta^{5+}, and S^{2-}, consistent with a Cu d^{10} valence band and a Ta d^0 conduction band. In contrast, Sunshine and Ibers[2] proposed that the valence states were likely to be Cu^{2+}Ta^{4+}S$_3$, similar to Cu$_{0.8}$Ta$_2$S$_6$.[30] They accounted for the low conductivity by assuming the unpaired electrons of Cu and Ta are sequestered in a strong Cu−Ta bond. Recent X-ray photoelectron spectroscopy (XPS)[1] and magnetic susceptibility[31] results, however, are consistent with our DFT calculations and assignment of formal oxidation states: Cu^{1+}Ta^{5+}S$_3$.

Optical and Electrical Properties of CuTaS$_3$. We evaluated optical properties by analysis of ground single crystals and thin films. Figure 4 shows a diffuse reflection spectrum of the ground crystals, revealing a band gap near 1 eV.
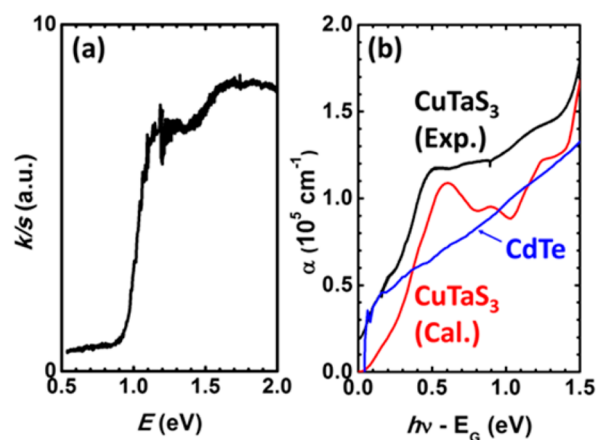

Figure 4. Optical absorption spectra from (a) diffuse reflectance of ground CuTaS$_3$ single crystals and (b) UV-NIR T-R measurments of a CuTaS$_3$ film. The absorption coefficient as a function of energy is compared to CdTe[32] and the computed spectrum of CuTaS$_3$. The sharp feature near 1.2 eV in (a) is an artifact of merging data sets from different optical detectors.

XRD analysis confirmed deposition of a crystalline CuTaS$_3$ film (Figure S1). The band gap and absorption coefficients were assessed from UV−vis−NIR transmittance (T) and reflectance (R) spectra. Absorption coefficients were calculated with eq 1,[32]

$$\alpha = \frac{1}{t} \ln \frac{(1 - R)^2}{T} \qquad (1)$$

which is applicable for large αd, i.e., $R^2 \exp(-2\alpha d) \ll 1$; t is the film thickness, 190 nm.

The band gap observed from the film is near 1 eV, consistent with the diffuse reflectance measurement (Figure 4). Figure 4 also shows a sharp absorption onset over a range of only 0.4 eV to an absorption coefficient exceeding 10^5 cm^{-1}. This onset and high absorption are consistent with the flat-band nature of the material observed in both the band-structure calculation (Figure 2) and the densities of states (Figure 3). The agreement of the observed and calculated absorption spectra (Figure 4) further reflects these results. The sharpness of the onset and the strength of the absorption exceed those of conventional solar absorbers such as CdTe (Figure 4).

The resistivity, $\rho_b = 2.1$ Ω cm, measured along [010] (*b* axis) of a single crystal is much smaller than that reported previously, >1.0 kΩ cm.[2] This discrepancy may arise from the nature of the contacts.[33] We employed Au contacts, while previous

researchers did not explicitly describe their contacts.[2] We did not measure the resistivity, ρ_{ac}, in the $a-c$ plane. The resistivity of pellets, $\rho_p = 0.4$ MΩ cm, prepared from ground crystals, however, is higher than ρ_b. ρ_p represents and average of ρ_b and ρ_{ac}. ρ_{ac} is anticipated to be higher than ρ_b based on the anisotropic nature of the crystal structure (Figure 1) and the band dispersion (Figure 3). Significant dispersion along [010] contributes to low ρ in the single crystal, while in pressed pellets, contributions from the flat, off-axis dispersion in the ac plane raises ρ.

The negative Seebeck coefficient, -1650 μV K^{-1}, of the pellets indicates electrons are majority carriers. This n-type behavior likely arises from sulfur vacancies or Ta-on-Cu antisites (Ta$_{Cu}$) defects, which place excess electrons in the Ta d conduction band. We attempted to force the material p-type by doping with Ti and Zr, but we observed only n-type behavior for samples doped to 3% of the Group 4 metal. The persistence of n-type behavior may be governed by small formation energies of the aforementioned defects.

Spectroscopic Limited Maximum Efficiency (SLME) for PV. We have employed the SLME metric[27] to assess the potential performance of CuTaS$_3$ as an absorber in a solar cell. SLME estimates cell performance based on the full absorption spectrum. It incorporates the type of transition, i.e., direct or indirect, and the magnitude of the band gap. It reflects both the absorption coefficient and the slope of the absorption onset. Figure 5 shows SLME values for CuTaS$_3$ and CuInSe$_2$ as a function of absorber thickness. Cells are predicted to reach 15% efficiency with 35 nm of CuTaS$_3$ and 75 nm of CuInSe$_2$.
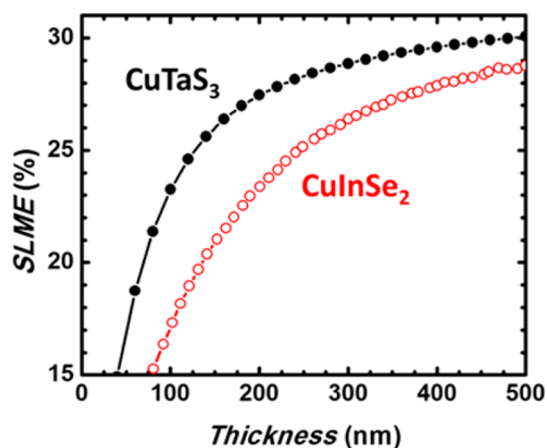

Figure 5. Calculated SLME values for CuTaS$_3$ as a function of film thickness, compared with CuInSe$_2$ calculated from data in ref 27.

Likewise, cells are predicted to reach 28% efficiency with 300 nm of CuTaS$_3$ and 500 nm of CuInSe$_2$. These results reflect the faster onset of the absorption coefficient to 10^5 cm^{-1} of CuTaS$_3$ ($\Delta E = 0.4$ eV) vs CuInSe$_2$ ($\Delta E = 1.5$ eV) and the higher maximum absorption coefficient of CuTaS$_3$. They also reflect the flat-band character of and the high joint density of states of CuTaS$_3$. In CuInSe$_2$, the CBM is characterized by a disperse In 5s band. This dispersion decreases the joint density of states of CuInSe$_2$ relative to CuTaS$_3$ and limits absorption.

This evaluation confirms that materials having intermetal d^0-d^{10} transitions can exhibit a strong onset coupled with high absorption. Such transitions need not be restricted to compounds containing a single d element. Also, CuTaS$_3$ may provide opportunities to realize high-efficiency thin-film solar

cells with ultrathin absorbers. The drift field across such ultrathin absorber layers should enhance photocarrier collection. The short drift length should also diminish the influence of defects on carrier recombination, assuming such thin films can be fabricated without pin holes. Hence, strong solar absorbers represent a unique approach to realize fundamental limits in PV performance, especially where maintaining a simple device design and structure is desired.[5,34]

CONCLUSIONS

We have identified the material CuTaS$_3$ via computational methods to be a strong solar absorber. CuTaS$_3$ exhibits metal d and sulfur p character near the band edges based on the two transition metals, i.e., Cu^{1+} (d^{10}) for VBM and Ta^{5+} (d^0) for CBM. These features contribute to a high joint density of states and favorable $p-d$ dipole matrix elements that produce an abrupt onset to an absorption coefficient > 10^5 cm^{-1} at E_g +0.4 eV. From the SLME calculation, the material is predicted to enable a high-efficiency (28%) thin-film solar cell with an absorber layer as thin as 300 nm. Strong absorption occurs via transition between two d metals, offering new design principles for solar absorbers, wherein (1) atomic solid-state energies guide selection of two metallic elements to produce a band gap aligned to the solar spectrum and (2) narrow d bands produce an abrupt onset to high absorption.

ASSOCIATED CONTENT

S **Supporting Information**

The Supporting Information is available free of charge on the ACS Publications website at DOI: 10.1021/acs.chemmater.6b04730.

Additional table and figures, including XRD, optical absorption coefficients, and EDX data (PDF)

AUTHOR INFORMATION

Corresponding Author

*(D.A.K.) E-mail: douglas.keszler@oregonstate.edu.

ORCID

Douglas A. Keszler: 0000-0002-7112-1171

Notes

The authors declare no competing financial interest.

ACKNOWLEDGMENTS

REFERENCES

(1) Cheng, D.; Jin, H.; Li, B.; Wang, X.; Chu, Q.; Lu, Y.; Liu, X.; Zhao, X. Structure Analysis of Needle-like Copper Tantalum Trisulfide Crystals by XPS and Raman Spectroscopy. *Chem. Res. Chinese Univ.* **2012**, *28* (2), 171−175.

(2) Sunshine, S. A.; Ibers, J. A. Redetermination of the Structures of CuTaS$_3$ and Nb$_2$Se$_9$. *Acta Crystallogr.* **1987**, *C43*, 1019−1022.

(3) Rose, A. A Global View of Solar Energy in Rational Units. *Phys. Stat. Sol. A* **1979**, *56*, 11−56.

(4) Green, M. A. *Third-Generation Photovoltaics: Advanced Solar Energy Conversion*; Springer: 2006.

(5) Heo, J.; Ravichandran, R.; Reidy, C. F.; Tate, J.; Wager, J. F.; Keszler, D. A. Design Meets Nature: New Tetrahedrtie Solar Absorbers. *Adv. Energy Mater.* **2015**, *5*, 1401506.

(6) Yu, L.; Lany, S.; Kykyneshi, R.; Jieratum, V.; Ravichandran, R.; Pelatt, B.; Altschul, E.; Platt, H. A. S.; Wager, J. F.; Keszler, D. A.; Zunger, A. Iron Chalcogenide Photovoltaic Absorbers. *Adv. Energy Mater.* **2011**, *1* (5), 748−753.

(7) Ennaoui, A.; Fiechter, S.; Goslowsky, H.; Tributsch, H. Photoactive Synthetic Polycrystalline Pyrite (FeS$_2$). *J. Electrochem. Soc.* **1985**, *132* (7), 1579−1582.

(8) Chatzitheodorou, G.; Fiechter, S.; Könenkamp, R.; Kunst, M.; Jaegermann, W.; Tributsch, H. Thin Photoactive FeS$_2$ (Pyrite) Films. *Mater. Res. Bull.* **1986**, *21*, 1481−1487.

(9) Tsai, M. L.; Su, S. H.; Chang, J. K.; Tsai, D. S.; Chen, C. H.; Wu, C. I.; Li, L. J.; Chen, L. J.; He, J. H. Monolayer MoS$_2$ Heterojunction Solar Cells. *ACS Nano* **2014**, *8* (8), 8317−8322.

(10) Shanmugam, M.; Bansal, T.; Durcan, C. A.; Yu, B. Molybdenum Disulphide/titanium Dioxide Nanocomposite-Poly 3-Hexylthiophene Bulk Heterojunction Solar Cell. *Appl. Phys. Lett.* **2012**, *100* (15), 153901.

(11) Shanmugam, M.; Durcan, C. A.; Yu, B. Layered Semiconductor Molybdenum Disulfide Nanomembrane Based Schottky-Barrier Solar Cells. *Nanoscale* **2012**, *4*, 7399−7405.

(12) Eyert, V.; Höck, K.-H.; Fiechter, S.; Tributsch, H. Electronic Structure of FeS$_2$: The Crucial Role of Electron-Lattice Interaction. *Phys. Rev. B: Condens. Matter Mater. Phys.* **1998**, *57* (11), 6350−6359.

(13) Kuc, A.; Zibouche, N.; Heine, T. Influence of Quantum Confinement on the Electronic Structure of the Transition Metal Sulfide TS2. *Phys. Rev. B: Condens. Matter Mater. Phys.* **2011**, *83* (24), 245213.

(14) Moore, C. E. *Atomic Energy Levels*; U.S. Government Printing Office: Washington, DC, 1949; Vol. *I*.

(15) Moore, C. E. *Atomic Energy Levels*; U.S. Government Printing Office: Washington, DC, 1952; Vol. *II*.

(16) Moore, C. E. *Atomic Energy Levels*; U.S. Government Printing Office: Washington, DC, 1958; Vol. *III*.

(17) Pelatt, B. D.; Ravichandran, R.; Wager, J. F.; Keszler, D. A. Atomic Solid State Energy Scale. *J. Am. Chem. Soc.* **2011**, *133* (42), 16852−16860.

(18) Pelatt, B. D.; Kokenyesi, R. S.; Ravichandran, R.; Pereira, C. B.; Wager, J. F.; Keszler, D. A. Atomic Solid State Energy Scale: Universality and Periodic Trends in Oxidation State. *J. Solid State Chem.* **2015**, *231*, 138−144.

(19) Haynes, W. M. *CRC Handbook of Chemistry and Physics*; CRC Press: 2005.

(20) Yanagi, T. *Arc Volcano of Japan*; Springer: 2011.

(21) Argus Media Company, Tantalum metal price resources. http://www.metal-pages.com/metalprices/tantalum/ (accessed Oct. 27, 2016).

(22) Blöchl, P. E. Projector Augmented-Wave Method. *Phys. Rev. B: Condens. Matter Mater. Phys.* **1994**, *50*, 17953−17979.

(23) Kresse, G.; Joubert, D. From Ultrasoft Pseudopotentials to the Projector Augmented-Wave Method. *Phys. Rev. B: Condens. Matter Mater. Phys.* **1999**, *59* (3), 1758−1775.

(24) Kresse, G.; Furthmüller, J. Efficient Iterative Schemes for Ab Initio Total-Energy Calculations Using a Plane-Wave Basis Set. *Phys. Rev. B: Condens. Matter Mater. Phys.* **1996**, *54* (16), 11169−11186.

(25) Heyd, J.; Scuseria, G. E.; Ernzerhof, M. Hybrid Functionals Based on a Screened Coulomb Potential. *J. Chem. Phys.* **2003**, *118* (18), 8207−8215.

(26) Shishkin, M.; Kresse, G. Self-Consistent GW Calculations for Semiconductors and Insulators. *Phys. Rev. B: Condens. Matter Mater. Phys.* **2007**, *75* (23), 235102.

(27) Yu, L.; Zunger, A. Identification of Potential Photovoltaic Absorbers Based on First-Principles Spectroscopic Screening of Materials. *Phys. Rev. Lett.* **2012**, *108* (6), 068701.

(28) Lake Shore. *7500/9500 Series Hall System User7s Manual*; 1994.

(29) Auparay, N. Room Temperature Seebeck Coefficient Measurement of Metals and Semiconductors. B.S. Thesis, Oregon State University, Corvallis, OR, June 2013.

(30) Squattrito, P. J.; Swepston, P. N.; Ibers, J. A. Crystal Structure of the New Ternary Chalcogenide [Tantalum Copper Sulfide] Ta$_2$Cu$_{0.80}$S$_6$. Relationship to Known Copper and Tantalum Chalcogenides. *Inorg. Chem.* **1987**, *26* (7), 1187−1188.

(31) Altschul, E. B. Transition Metal Solar Absorbers. M.S. Thesis, Oregon State University, Corvallis, OR, June 2012.

(32) Adachi, S. *Optical Constants of Crystalline and Amorphous Semiconductors*; Springer: 1999.

(33) Segawa, K.; Ando, Y. Transport Anomalies and the Role of Pseudogap in the 60-K Phase of YBa$_2$Cu$_3$O$_{7-\delta}$. *Phys. Rev. Lett.* **2001**, *86* (21), 4907−4910.

(34) Yu, L.; Kokenyesi, R. S.; Keszler, D. A.; Zunger, A. Inverse Design of High Absorption Thin-Film Photovoltaic Materials. *Adv. Energy Mater.* **2013**, *3* (1), 43−48.